Emergent perpendicular magnetic anisotropy at the interface of an oxide heterostructure

Chuangye Song,[1,2] Xuanyi Li,[2,3] Lvkang Shen,[4] Baoshan Cui,[1,2] Xing Xu,[1] Guoqiang Yu,[1,2,3] Ming Liu,[4] Sheng Meng,[1,2,3,*] and Kehui Wu[1,2,3,†]

[1]*Songshan Lake Materials Laboratory, Dongguan, Guangdong 523808, China*
[2]*Institute of Physics, Chinese Academy of Sciences, Beijing 100190, China*
[3]*School of Physics, University of Chinese Academy of Sciences, Beijing 100049, China*
[4]*School of Electronic and Information Engineering, Xi'an Jiaotong University, Xi'an 710049, China*

(Received 21 December 2020; revised 24 May 2021; accepted 1 September 2021; published 28 September 2021)

Controlling the magnetic anisotropy in magnetic oxides is critical for the development of oxide spintronics. Here we report on the finding of an emergent interfacial magnetism, with unique perpendicular magnetic anisotropy (PMA), at the interface of a half-doped manganite $La_{1/2}Sr_{1/2}MnO_3$ film on $LaAlO_3$ substrate, through combined electron spin resonance measurements and density functional theory calculations. The interfacial magnetism can be explained by the $3d_{3z^2-r^2}$ orbital-mediated ferromagnetic exchange interaction between Mn ions near the interface, which is enhanced by the compressive strain from the substrate. Our results provide a useful PMA system for possible spintronic applications, as well as atomistic-level insight to the magnetic anisotropy in strained manganite oxide interfaces.

DOI: 10.1103/PhysRevB.104.115162

I. INTRODUCTION

Magnetism in transition metal oxides (TMOs) has attracted growing interest as it offers the possibility to integrate spintronic devices with the rich exotic properties of TMOs, such as high spin polarization, superconductivity, and ferroelectricity. One of the key issues in understanding and utilizing the magnetism in TMOs is the magnetic anisotropy (MA), which describes the easy arrangement of spins along a specific direction. The MA determines a variety of physical phenomena including magnetocaloric effects [1] and Kondo effects [2]. In particular, perpendicular magnetic anisotropy (PMA), where the easy magnetization axis points perpendicular to a film surface, is highly desired in data storage and logic devices as it enables magnetization switching triggered by a spin current with a low current density [3,4]. In addition, competition between PMA and other mechanisms (e.g., Dzyaloshinskii-Moriya interaction) gives rise to interesting spin textures [5], including chiral domain walls, magnetic skyrmions [6], and topological phenomena [7]. Therefore, it is of great importance to understand and control the formation of PMA in magnetic oxide materials.

The half-doped perovskite manganite $La_{1/2}Sr_{1/2}MnO_3$ (LSMO), which lies in the boundary between ferromagnetic/antiferromagnetic phases [8], possesses strong electron correlation and exhibits intriguing multiple ground states [9] and metal-insulator transition (MIT) [10]. The MIT in LSMO manifests competition between ferromagnetic (FM) double exchange and antiferromagnetic (AFM) superexchange interactions, accompanied with rich spin configurations. However, like other TMO thin films, LSMO thin films normally show an in-plane MA due to the shape anisotropy [11]. Recently, successful approaches to tune the MA in $3d$ TMOs, including liquid-ionic gating [12], tilted oxygen octahedron [13,14], and symmetry mismatch [15] have been reported. These methods explore the possibility to control the MA in TMO thin films by tuning the electron density of states, oxygen vacancies, or distortion of the oxygen octahedrons in the lattice. However, they typically require high-quality epitaxial superlattice, or an external-field manipulation. More effective approaches toward PMA are still desirable to date.

In this work, we report a simple strategy to realize PMA in LSMO films. We found that PMA can be created at the interface between a LSMO film and $LaAlO_3$ (LAO) substrate by the epitaxial strain. The magnetism of oxide interfaces has been rarely studied previously, since the interfacial spin component is too small to be detectable with conventional measurement facilities. Herein, we employed the electron spin resonance (ESR) spectrum to explore tiny signals hidden at the interface and that of the bulk LSMO films, simultaneously. The microscopic origin of PMA at the interface can be well explained by the strain-modulated magnetic anisotropy energy (MAE) and orbital occupancies, as corroborated by high-resolution transmission electron microscopy (TEM) study and density functional theory (DFT) calculations. In addition, we also discovered narrow resonant lines superimposed on the broader resonance peak during PM/FM phase transitions, which suggests the emergence of locally ordered "superspins." Our work provides a simple approach to engineer the interface magnetism in magnetic oxides.

II. RESULTS AND DISCUSSION

Epitaxial LSMO film with thickness of ∼120 nm was grown on perovskite (001)-oriented LAO substrates by pulsed laser deposition (PLD) at 800 °C. The laser energy density

*Corresponding author: smeng@iphy.ac.cn
†Corresponding author: khwu@iphy.ac.cn

 ©2021 American Physical Society

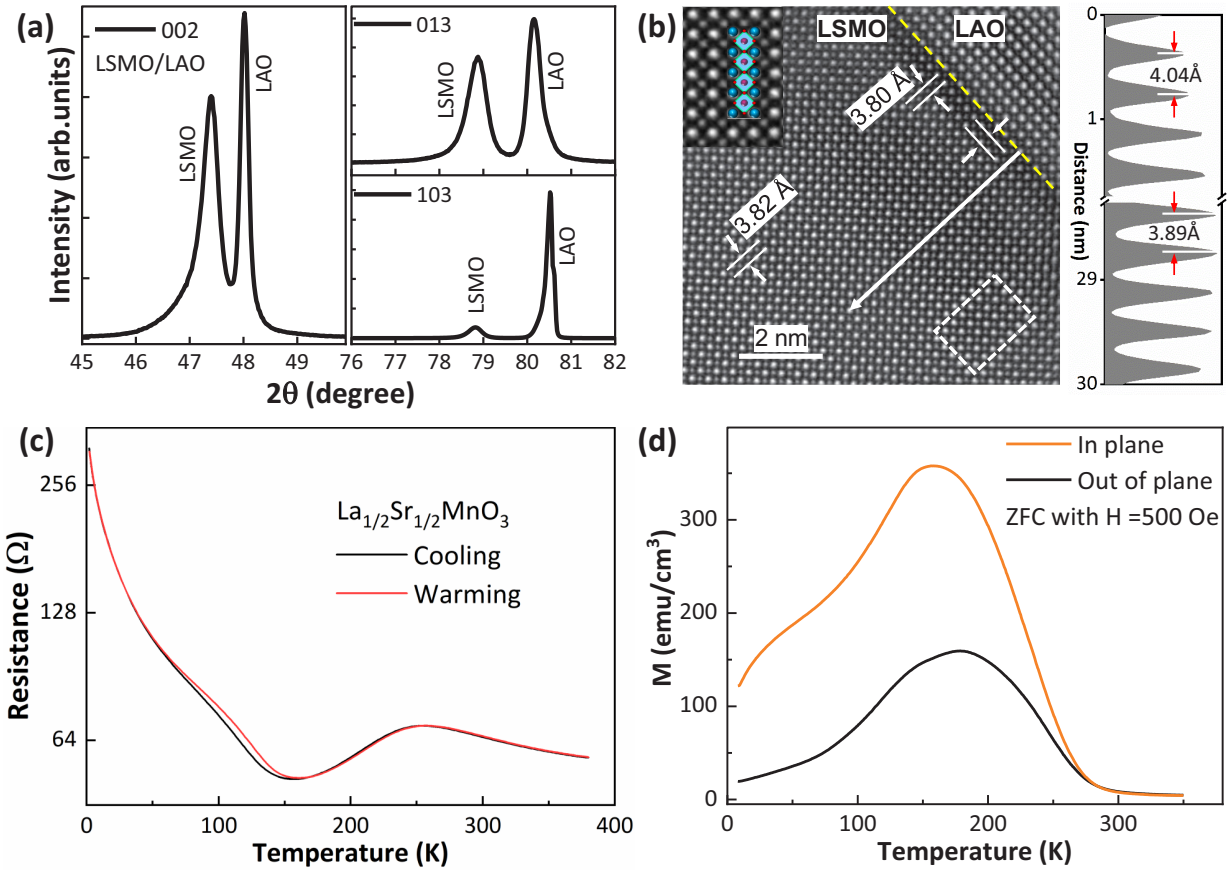

FIG. 1. Crystallographic structure and electrical/magnetic characterization. (a) XRD diffraction patterns of epitaxial LSMO films grown on LAO substrate around the (002), (013), and (103) Bragg planes. (b) Left: Fourier-filtered HAADF micrograph of the LSMO film on LAO substrate taken by an aberration-corrected STEM. Right: Intensity line profile along the white arrow. Inset shows the zoom-in of the rectangular area. (c) Temperature-dependent resistance goes through two pronounced metal-insulator transitions. The red curve shows the warming process and black curve shows the cooling process. (d) Temperature-dependent magnetization (M) measured during warming with 500 Oe magnetic field (H) applied along in-plane (orange) and out-of-plane (black) after zero-field-cooling (ZFC).

was about $2\,\mathrm{J\,cm^{-2}}$ with the repetition rate of 3 Hz. The oxygen pressure was maintained at 20 Pa during the growth. X-ray diffraction (XRD) measurement shows the same set of sharp peaks from LSMO as that from the LAO substrate, indicating the high quality of epitaxial growth. In addition, each peak from LSMO locates at the left side of the corresponding LAO peak, consistent with the fact that LSMO has larger lattice constants than those of LAO; see Fig. 1(a). The lattice mismatch between LSMO and LAO indicates that the LSMO film would be compressively strained at the interface. To further examine the interfacial crystallinity, high-resolution TEM measurement was performed, as shown in Fig. 1(b). The Fourier-filtered high-angle annular dark-field (HAADF) micrograph manifests a well-defined, atomically sharp interface (yellow dash line). The in-plane lattice constant in the LSMO side at the interface is measured to be 3.80 ± 0.01Å, close to that of LAO substrate. It continuously relaxes to 3.82 $\pm$ 0.01Å at about 7 nm away from the interface [Fig. 1(b)], and further to 3.85 ± 0.01 Å at about 20 nm away from the interface (not shown in the figure). Because the in-plane lattice constant of bulk LSMO (3.85 Å) is about 1.7% larger than that of LAO substrate (3.79 Å), in-plane compressive strain should be generated in the LSMO film close to the interface region. This can also be confirmed by the line profile along the direction perpendicular to the interface [white arrow direction in Fig. 1(b)], which reveals that the lattice spacing along the c axis is larger at the interface ($d = 4.04 \pm 0.01$ Å) than in bulk film ($d = 3.85 \pm 0.01$ Å); the lattice expansion along c axis is consistent with the in-plane compression. In brief, the TEM measurement indicates an atomically sharp interface and about a 20-nm-thick, compressively strained interface region in the LSMO film.

The temperature-dependent resistance measurement reveals two MITs, as shown in Fig. 1(c). The resistance maximum around 257 K corresponds to the first MIT, a paramagnetism (PM) to FM transition during cooling. During a typical PM to FM transition, randomly distributed FM domains and boundaries are initially created, which hinder the electron transport and result in the increase of resistivity. However, with further decreasing temperature, the FM domains align and grow in size, and the reduced density of FM domain boundaries results in the decrease of resistivity. Therefore, there exists a resistivity maximum corresponding to a maximal density of FM domain boundaries. Meanwhile, the

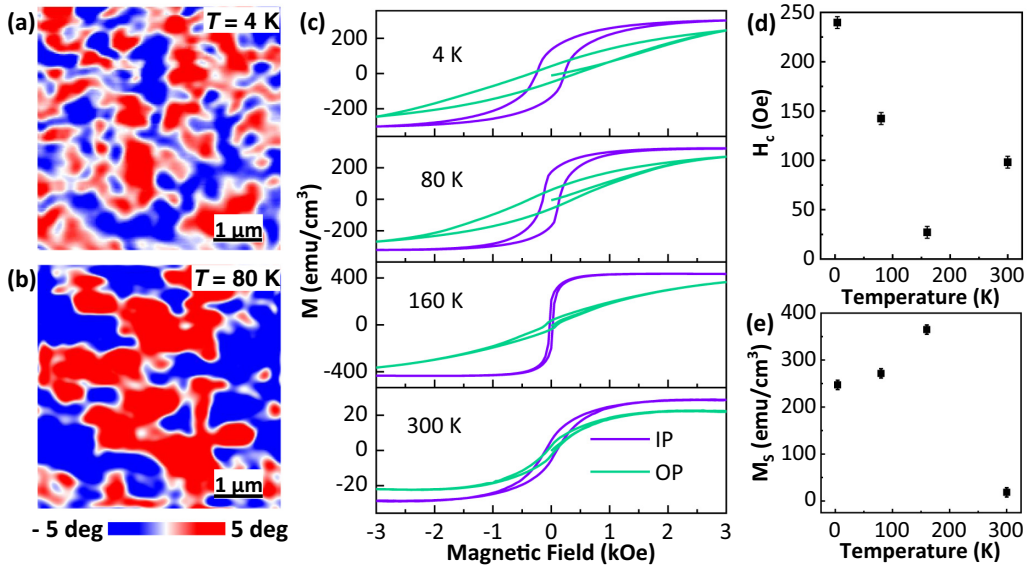

FIG. 2. Characterization of magnetic properties of LSMO films. MFM measurement of the LSMO film at $T = 4$ K (a) and $T = 80$ K with $H = 0$ T; the positive (red) and negative (blue) signals are representative of magnetic domain patterns. (c) Magnetization as a function of magnetic field, for fields applied in both in-plane (IP) and out-of-plane (OP) directions. The magnetization is dominated by the bulk and exhibits a typical in-plane magnetic anisotropy. Panels (d) and (e) are coercive field (H_c) and saturated magnetization (M_s), respectively, extracted from (c).

resistivity minimum around 166 K corresponds to the completion of the PM-FM transition and the highest- purity FM phase. The second MIT occurs below 166 K, where further lowering the temperature will cause the transition from FM phase to phase-separated FM/AFM phase, and correspondingly an increasing resistivity. The almost identical curves observed during warming and cooling indicate that the two MITs are reversible. These observations are in agreement with previous reports [16]. The above picture is also consistent with the temperature dependence of magnetization curves measured during warming under 500 Oe after zero field cooling [Fig. 1(d)]. Here the magnetization above 320 K goes to nearly zero, indicating a paramagnetism above that temperature. On the other hand, the pronounced magnetization from 300 to 166 K indicates the emergence of FM in the sample. Finally, the magnetization is obviously suppressed below 166 K, which is in accordance with the existence of an AFM/FM phase-separated ground state.

The suppression of magnetization at low temperature can be further confirmed by our magnetic force microscopy (MFM) observations as shown in Figs. 2(a) and 2(b). For the MFM images, the areas with negative-phase (blue) and positive-phase (red) signals represent ferromagnetic domains. It is notable that the ferromagnetic domains grow in size with enhanced contrast upon warming from 4 to 80 K, which is attributed to the increased volume fraction of the FM phase in the AFM/FM phase separated state. This can also account for the monotonically increasing resistivity with decreasing temperature below 166 K [Fig. 1(c)]. Figure 2(c) depicts the measured magnetization as a function of the magnetic field in both in-plane and out-of-plane directions. At the whole temperature range, the in-plane *M-H* hysteresis loop exhibits higher remanence and lower saturation fields as compared to the out-of-plane *M-H* curves, confirming the presence of in-plane magnetic anisotropy. Moreover, as the temperature decreases from 300 to 4 K [from bottom to top panels in Fig. 2(c)], the coercive field initially decreases, and then increases with decreasing temperature. Correspondingly, the saturated magnetization is first enhanced and then suppressed with lowering the temperature. This is in very good accordance with the above discussed phase transition diagram: The *M-H* curve at 160 K corresponds to the highest purity FM phase, while the *M-H* curves at 80 and 4 K correspond to phase-separated FM/AFM phases. Notably, the *M-H* curve at 300 K exhibits a weak but clear hysteresis loop, indicating the presence of the FM phase already at this high temperature. The extracted coercive field (H_c) and saturation field (M_s) from the curves in Fig. 2(c) are plotted in Figs. 2(d) and 2(e), respectively.

In the above magnetic property measurements, the magnetization signals are dominated by the bulk properties. To study the magnetism at the interface, we performed ESR measurements with microwave frequency $\nu = 9052.939$ MHz by using a BRUKER ER-200D spectrometer, within the temperature $4\ \mathrm{K} < T < 321$ K. The ESR technique facilitates the study of spin dynamics in manganite oxides [17,18] since it is sensitive to all spin resonant modes including the body spin-wave mode, interface spin-wave mode, and uniform-precession mode [19]. In general, for a paramagnetic (PM) material, the resonant signal is a symmetric peak centered at

$$H_0^{\mathrm{PM}} = \omega/\gamma, \tag{1}$$

where ω is the angular frequency of the microwave, γ is the gyromagnetic ratio ($\gamma = 2\pi g_{\mathrm{eff}}\mu_B/\hbar$), where $\hbar$ is Planck's constant and μ_B is the Bohr magneton. In principle the value of H_0^{PM} has no dependence on temperature or magnetic-field direction. However, experimentally a slight shift of the peak

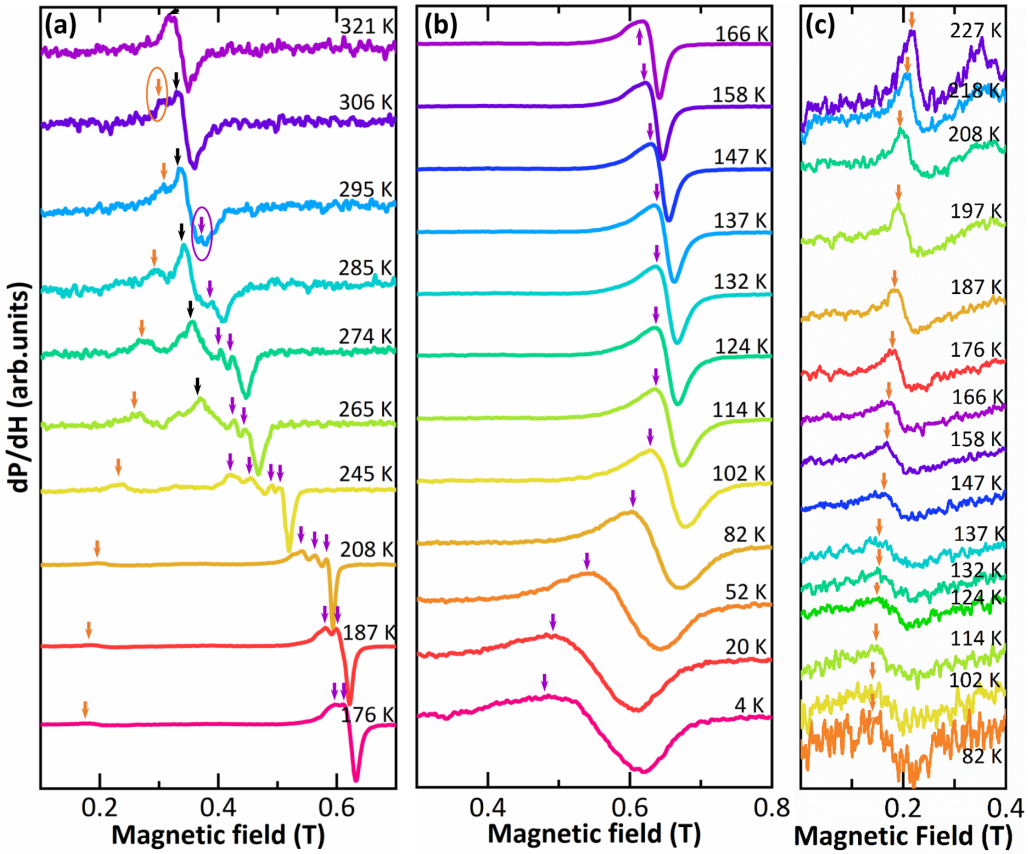

FIG. 3. Spin resonance with H applied perpendicular to the film plane. (a),(b) Differential ESR absorption dP/dH vs H at different temperature measured during warming. H is applied perpendicular to the film plane. Black, purple, and orange arrows are used to label the resonant peaks from paramagnetic bulk, ferromagnetic bulk, and interface magnetism. The starting of resonances from interfacial and bulk are indicated by an orange and a purple solid circle, respectively. Note that the intensity of different curves is normalized for a convenient alignment of different curves, but the curves in middle temperature range have much stronger resonance signals. (c) Enlarged view of the spin excitation of the interfacial magnetism. Note that for a better view, the position of the resonance peaks is marked at the position of the left shoulder in the differential curves instead of at the center of the peak.

with temperature may be found due to the inhomogeneity of the film during PM-FM phase transition [20,21]. For ferromagnetic materials, at temperature below T_c, the magnetic resonance is governed by the spontaneous magnetization M_0 as well as anisotropies due to the presence of shape and strain [18]. Generally, the Kittel formulas [22] with appropriate demagnetizing field and magnetoelastic coupling field are adopted to describe the resonance in ferromagnetic thin films:

$$(\omega/\gamma)^2 = [H_0^{\perp} - 4\pi M_0 + 2B_1(e_{zz} - e_{xx})/M_0] \times [H_0^{\perp} - 4\pi M_0 + 2B_1(e_{xx} - e_{yy})/M_0], \quad (2)$$

$$(\omega/\gamma)^2 = [H_0^{\parallel} + 2B_1(e_{zz} - e_{xx})/M_0] \times [H_0^{\parallel} + 4\pi M_0 - 2B_1(e_{yy} + e_{xx})/M_0], \quad (3)$$

where $H_0^{\perp}$ and $H_0^{\parallel}$ are resonance fields for H perpendicular and parallel to the film plane, respectively, $4\pi M_0$ is the demagnetization field due to the film shape, B_1 is the longitudinal magnetoelastic coupling constant, and e_{xx}, e_{yy}, and e_{zz} are the components of the strain tensor along [100], [010], and [001], respectively [23]. According to Eqs. (2) and (3), the magnetic anisotropy of the film is a combined effect of the demagnetization and magnetoelastic coupling. For a strain-relaxed bulk FM, the strain tensors $e_{xx} = e_{yy} = e_{zz}$, and the magnetoelastic coupling constant $B_1 = 0$. The above formulas can be simplified as

$$\omega/\gamma = H_0^{\perp} - 4\pi M_0, \quad (4)$$

$$(\omega/\gamma)^2 = H_0^{\parallel}(H_0^{\parallel} + 4\pi M_0). \quad (5)$$

Figure 3 plots the measured ESR resonance (differential absorption dP/dH versus H) at different temperatures from 321 to 4 K, with magnetic field applied perpendicular to the film plane. At 321 K, the curve exhibits a single peak, marked by black arrow, in Fig. 3(a). From the previous discussed phase diagram, our sample is paramagnetic at 321 K. Thus, we attribute this peak to the resonance from the PM phase. This peak remains roughly in the same position as the temperature decreases, which is characteristic of a PM resonance. And it diminishes around 265 K, in accordance with the survival temperature region of the PM phase in our sample. The dominant feature in Fig. 3 is that below 285 K, a strong resonance peak appears at higher magnetic field. The resonance field initially increases (before reaching 158 K), and then decreases with

decreasing temperature. According to the phase diagram in our sample, this resonance most likely comes from the ferromagnetic bulk. As we have discussed in the magnetization curve in Fig. 1(d), the emergence of ferromagnetism in our sample from 300 to 166 K is accompanied by the increase of magnetization, and the transition to a mixture of FM/AFM phase below 166 K will cause a decrease of magnetization. The coherent temperature dependence of the resonance field and magnetization is in good agreement with Eq. (4), $\omega/\gamma = H_0^{\perp} - 4\pi M_0$. Here, as ω/γ is fixed, the resonance field has a linear dependence of the magnetization M_0. This further supports the assignment of this peak to FM resonance. In the following we use $\mathrm{FM_{bulk}}$ to denote this FM phase.

In addition, we find that the ferromagnetic resonance lines comprise a superposition of a few narrower lines, which pop up one by one when lowering the temperature. Their quantity gradually descends and transforms into a broad one at 166 K. These fine structures indicate that the bulk FM phase is inhomogeneous, e.g., because it occupies regions of irregular shape and/or other local "superspin" phases present. The inhomogeneity evolves with temperature and transfer to a pure FM phase with improved conductivity. Finally, the linewidth begins to broaden, accompanying a transition to mixed FM/AFM phases.

The most interesting observation in the above experiment is that at 306 K and below, another signature of ferromagnetic resonance, as marked by orange arrows, appears at the lower magnetic field region, distinct from that of the bulk FM lines. Moreover, the resonance field of this peak moves to the lower region as the temperature decreases, exhibiting an opposite temperature dependence to the bulk FM lines. The completely different field and temperature dependence indicates that this resonance is not from the bulk. We suggest that it most likely comes from the strained part of the LSMO film near the interface, as this is the only other source of magnetism. As the LSMO/LAO interface has nonzero strain, Eq. (4) is no longer applicable, and one has to go back to Eq. (2). For an in-plane compressive strain in this region, we have $e_{xx} = e_{yy} = e_{\mathrm{in}} < 0$, and $e_{zz} = e_{\mathrm{out}} > 0$; the free energies along [100] and [001] axis are $F_{[100]} = B_1 e_{xx}$ and $F_{[001]} = B_1 e_{zz}$, respectively. From Eq. (2) we deduce

$$({}^{\omega}/_{\gamma})^2 = (H_0^{\perp} - 4\pi M_0 + 2B_1(e_{zz} - e_{xx})/M_0)(H_0^{\perp} - 4\pi M_0).$$

As we observe $H_{\perp}^{\mathrm{FM}} < \omega/\gamma$ for the interface ferromagnetism, the term $2B_1(e_{zz} - e_{xx})/M_0$ has to be negative, i.e., $B_1 < 0$ and $F_{[001]} < F_{[100]}$. Thus, the energy minima of this interfacial counterpart locate along out of plane, indicating that we have a PMA at the interface. Here we denote this interfacial phase as $\mathrm{FM_{inter}}$. This FM resonance persists down to our lowest measurement temperature [see the zoom-in feature of this resonance in Fig. 3(c)]. Thus, two distinct magnetisms, interfacial and bulk, are revealed by the ESR measurement.

The above picture is further supported by ESR measurements performed with H applied parallel to the film plane [Fig. 4(a)]. In this case, the $\mathrm{FM_{bulk}}$ and $\mathrm{FM_{inter}}$ lines interchange based on Eqs. (3) and (5) such that $H_{\parallel}^{\mathrm{FM_{bulk}}} < H_0^{\mathrm{PM}}$ and $H_{\parallel}^{\mathrm{FM_{inter}}} > H_0^{\mathrm{PM}}$. The signal from the interfacial counterpart is marked by a red arrow [see Fig. 4(b) for details], while the signal from the bulk magnetism (purple arrow) locates at lower

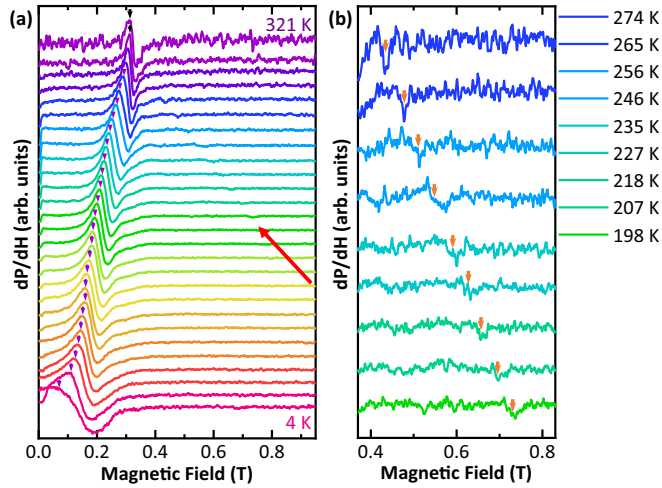

FIG. 4. Spin excitations with H applied parallel to the film plane. (a) Differential absorption dP/dH vs H at different temperature measured during warming. H is applied parallel to the film plane; the signal from the interfacial and bulk counterparts are marked by red and purple arrows, respectively. (b) Enlarged view of the spin excitation of the interfacial magnetism.

field. On the other hand, the resonant signal corresponding to the PM phase at the high temperature regime is also observed, as marked by a black arrow in Fig. 4(a). This peak position is in agreement with the measurement performed with H applied perpendicular to the film plane [Fig. 3(a)]. However, as the FM resonance moves to the lower field region in this case, it is harder to distinguish the PM signal from the intensive FM signal at lower temperature range.

To dig out more information from the measured resonance curves, the peak-to-peak linewidth of the FM resonance peak, ΔH_{pp}, defined as the width between the highest point and the lowest one in the ESR spectrum, has been extracted from the curves in Fig. 3. The linewidth of the FM resonance peak is related to the degree of inhomogeneity in local magnetization [18]. The linewidth of bulk FM phase, $\Delta Hpp^{\mathrm{FM_{bulk}}}$, becomes smaller below T_c as a result of local magnetic domain permeation and improved homogeneity upon cooling. As shown in Fig. 5(a), the temperature dependent resonance linewidth illustrates the evolution of magnetic domain size with the temperature. The linewidth evolution as a function of temperature shows an almost identical trend as that of the temperature-dependent resistivity curve in Fig. 1(c). Both the resistivity curve and resonance linewidth show a bump at 257 K, and a monotonic increase with decreasing temperature below 166 K. This indicates that the creation of random FM domains or intermixing FM/AFM domains, both causing the increasing resistivity, will also hinder the propagation of spin waves and result in broaden resonance linewidth.

The magnetic anisotropy in different phases can be characterized by the magnetic anisotropy field $H_{\mathrm{anis}} = (H_0^{\perp} - H_0^{\parallel})$ [24,25], as derived from Figs. 3 and 4 and plotted in Fig. 5(b). The bulk magnetism has a positive H_{anis}, indicating in-plane magnetic anisotropy, which is in accordance with field dependent magnetization [Fig. 2(c)]; while the interfacial magnetism possesses a strongly negative H_{anis} and a PMA.

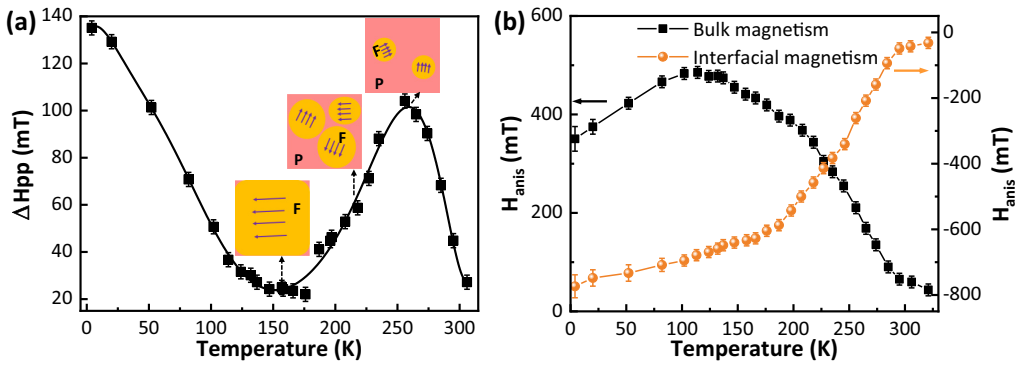

FIG. 5. Phase inhomogeneity and distinct magnetic anisotropies. (a) The temperature dependent linewidth $\Delta H_{pp}^{\mathrm{FM_{bulk}}}$ for H applied perpendicular to the film plane. Inset shows the schematics of the several ground states across the PM/FM phase transition, illustrating the evolution of magnetic domain size with the temperature. The purple arrows represent the locally ordered spins of individual domain. F ferromagnetic state, P paramagnetic state. (b) Temperature-dependent magnetic anisotropy field H_{anis} of the bulk (black) and interfacial (orange) magnetism.

According to Eqs. (2) and (3), we suggest that the demagnetization field ($4\pi M_0$) determines the magnetic anisotropy in bulk phase, whose H_{anis} has the same tendency with magnetization. For the interfacial phase, the magnetoelastic field should play an important role in the appearance of PMA, which has been found in several metallic magnets [26,27].

To understand the microscopic origin of this dramatic interface PMA, we performed DFT calculations using the generalized gradient approximation (GGA) and the projector augmented wave (PAW [28]) method as implemented by the Vienna *ab initio* simulation package (VASP [29]). The $7 \times 7 \times 5$ k-point mesh generated by Monkhost-Pack was used in geometry relaxation and all atomic positions of LSMO supercell were fully relaxed with the maximal Hellmann-Feynman force on each atom less than 10^{-3} eV/A and free energy less than 10^{-5} eV. The energy cutoff for the expansion of the plane wave basis was set to be 500 eV [30]. We use the Perdew-Burke-Ernzerhof (PBE [31]) functions with the inclusion of spin orbit coupling when calculating the magnetic anisotropy energies (MAE), which was gained by rotating the spin orientation from the x-y plane ($E_{\parallel}$) to the z axis ($E_{\perp}$) [13].We built a $\sqrt{2} \times \sqrt{2} \times 2$ $SrMnO_3$ supercell with half of the Sr atoms replaced by La atoms to satisfy the $La_{0.5}Sr_{0.5}MnO_3$ doping and space group $I\bar{4}2m$. The magnetic anisotropy energies MAE $= E_{\perp} - E_{\parallel}$ (MAEs) of the LSMO film as a function of the lattice distortion were calculated, and the results are depicted in Fig. 6(a). Here $c/a < 1$ corresponds to in-plane tensile strain and $c/a > 1$ to compressive strain, respectively. It is clearly shown that in-plane tensile strain ($c/a < 1$) induces a positive MAE, corresponding to a more stable in-plane magnetization, while compressive strain ($c/a > 1$) induces a negative MAE, indicating that perpendicular magnetization is preferred.

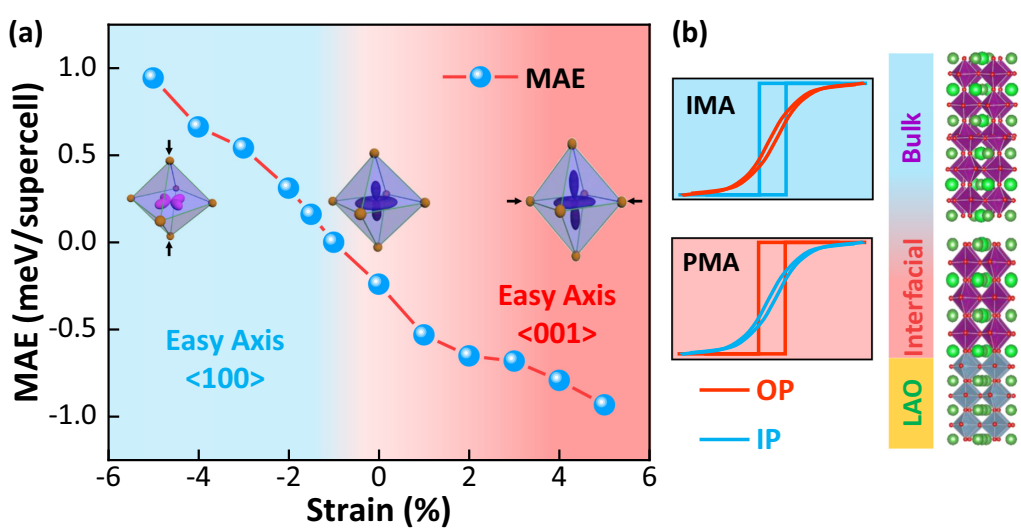

FIG. 6. Mechanism of the interfacial PMA phase. (a) Strain-dependent magnetic anisotropy energy by DFT calculations indicates an orbital-mediated ferromagnetic double-exchange and magnetic anisotropy. (b) The magnetic hysteresis loops are schematically shown for the PMA at the interface and in-plane magnetic anisotropy (IMA) for the bulk film counterparts, with external field applied along in-plane (IP) and out-of-plane (OP), respectively. Strain from the LAO substrate induces c-axis lattice tension in the LSMO film near the interface, while the lattice recovers to the initial symmetry when the strain is released.

Hence, we prove that the compressive strain from the LAO substrate is the origination of PMA at the interface. To better understand this picture, it can be imagined that compressive strain will induce the elongation of oxygen octahedral along the c axis. This can introduce the redistribution of electrons in Mn^{3+}/Mn^{4+} cations favoring the occupation of $3d_{3z^2-r^2}$-dominated e_g orbitals, which in turn will enhance the FM coupling of spins in neighboring Mn atoms [32]. To illustrate this more clearly, the structural evolution of a LSMO film is shown schematically in Fig. 6(b), demonstrating a PMA in the strained interfacial LSMO and the in-plane magnetic anisotropy in the strain-relaxed bulk LSMO films. Thus, the $3d_{3z^2-r^2}$ electrons with orbital anisotropy participate in the ferromagnetic exchange interactions and contribute a lot to the interfacial magnetism with PMA. Further away from the interface region, the strain-relaxed LSMO possesses the perfect manganite crystal structure, tending to form an in-plane magnetic anisotropy due to shape anisotropy in thin films.

III. CONCLUSIONS

To conclude, a strain-driven magnetic anisotropy at the interface of an oxide heterostructure is indicated via a combination of ESR spectra, XRD, TEM, and DFT calculations. Compressive strain leads to a $3d_{3z^2-r^2}$-dominated ferromagnetic exchange interaction and introduces an interfacial magnetism with unique PMA. Thus, we demonstrate strain as an effective tuning parameter to achieve PMA at an oxide interface, and this strategy can be extended to a wider class of interface engineering for spintronic device applications. Since the easy magnetization axis of the bulk and interface phases are perpendicular to each other, one can expect that the interfacial PMA could be independently modulated under various stimuli (e.g., epitaxial strain, electric and magnetic field).

ACKNOWLEDGMENTS

This work was supported by the National Natural Science Foundation of China (Grants No. 11825405 and No.1192780039), the Ministry of Science and Technology of China (Grant No. 2016YFA0300904), and the Strategic Priority Research Program of the Chinese Academy of Sciences (Grant No. XDB30000000). C.S. acknowledges support from the China Postdoctoral Science Foundation (Grant No. 2020M670502), and the Guangdong Basic and Applied Basic Research Foundation (Grant No. 2021A1515010030).

K.W. and C.S. conceived the experiments and prepared the manuscripts. C.S. prepared the thin films and performed the ESR measurement. X.L. and S.M. performed the DFT calculations. L.S. and M.L. helped analyze the ESR data. C.S. and X.L. contributed equally to this work. All authors were involved in the discussion and revision of the manuscript.

The authors declare no competing interests.

[1] M. S. Reis, R. M. Rubinger, N. A. Sobolev, M. A. Valente, K. Yamada, K. Sato, Y. Todate, A. Bouravleuv, P. J. von Ranke, and S. Gama, Phys. Rev. B **77**, 104439 (2008).

[2] A. F. Otte, M. Ternes, K. von Bergmann, S. Loth, H. Brune, C. P. Lutz, C. F. Hirjibehedin, and A. J. Heinrich, Nat. Phys. **4**, 847 (2008).

[3] B. Dieny and M. Chshiev, Rev. Mod. Phys. **89**, 025008 (2017).

[4] P. Li, T. Liu, H. Chang, A. Kalitsov, W. Zhang, G. Csaba, W. Li, D. Richardson, A. DeMann, G. Rimal, H. Dey, J. S. Jiang, W. Porod, S. B. Field, J. Tang, M. C. Marconi, A. Hoffmann, O. Mryasov, and M. Wu, Nat. Commun. **7**, 12688 (2016).

[5] Wenbo Wang, M. W. Daniels, Z. Liao, Y. Zhao, J. Wang, G. Koster, G. Rijnders, C. Chang, D. Xiao, and W. Wu, Nat. Mater. **18**, 1054 (2019).

[6] U. K. Rößler, A. N. Bogdanov, and C. Pfleiderer, Nature (London) **442**, 797 (2006).

[7] N. Nagaosa and Y. Tokura, Nat. Nanotechnol. **8**, 899 (2013).

[8] J. Hemberger, A. Krimmel, T. Kurz, H. A. Krug von Nidda, V. Y. Ivanov, A. A. Mukhin, A. M. Balbashov, and A. Loidl, Phys. Rev. B **66**, 094410 (2002).

[9] D. Gutiérrez, G. Radaelli, F. Sánchez, R. Bertacco, and J. Fontcuberta, Phys. Rev. B **89**, 075107 (2014).

[10] Y. Konishi, Z. Fang, M. Izumi, T. Manako, M. Kasai, H. Kuwahara, M. Kawasaki, K. Terakura, and Y. Tokura, J. Phys. Soc. Jpn. **68**, 3790 (1999).

[11] S. Lin, Q. Zhang, M. A. Roldan, S. Das, T. Charlton, M. R. Fitzsimmons, Q. Jin, S. Li, Z. Wu, S. Chen, H. Guo, X. Tong, M. He, C. Ge, C. Wang, L. Gu, K. J. Jin, and E. J. Guo, Phys. Rev. Appl. **13**, 034033 (2020).

[12] B. Cui, C. Song, G. A. Gehring, F. Li, G. Wang, C. Chen, J. Peng, H. Mao, F. Zeng, and F. Pan, Adv. Funct. Mater. **25**, 864 (2015).

[13] X. Chen, S. Zhang, B. Liu, F. Hu, B. Shen, and J. Sun, Phys. Rev. B **100**, 144413 (2019).

[14] D. Yi, C. L. Flint, P. P. Balakrishnan, K. Mahalingam, B. Urwin, A. Vailionis, A. T. N'Diaye, P. Shafer, E. Arenholz, Y. Choi, K. H. Stone, J. H. Chu, B. M. Howe, J. Liu, I. R. Fisher, and Y. Suzuki, Phys. Rev. Lett. **119**, 077201 (2017).

[15] J. Zhang, Z. Zhong, X. Guan, X. Shen, J. Zhang, F. Han, H. Zhang, H. Zhang, X. Yan, Q. Zhang, L. Gu, F. Hu, R. Yu, B. Shen, and J. Sun, Nat. Commun. **9**, 1923 (2018).

[16] C. Song, I. A. Malik, M. Li, Q. Zhang, L. Wang, J. Wang, R. Chen, R. Zheng, S. Dong, L. Gu, W. Duan, C. Nan, and J. Zhang, Sci. China Mater. **62**, 577 (2019).

[17] S. Emori, U. S. Alaan, M. T. Gray, V. Sluka, Y. Chen, A. D. Kent, and Y. Suzuki, Phys. Rev. B **94**, 224423 (2016).

[18] A. I. Tovstolytkin, V. V. Dzyublyuk, D. I. Podyalovskii, X. Moya, C. Israel, D. Sánchez, M. E. Vickers, and N. D. Mathur, Phys. Rev. B **83**, 184404 (2011).

[19] M. Zhu, Z. Zhou, B. Peng, S. Zhao, Y. Zhang, G. Niu, W. Ren, Z. Ye, Y. Liu, and M. Liu, Adv. Funct. Mater. **27**, 1605598 (2017).

[20] L. Chen, J. Fan, W. Tong, D. Hu, Y. Ji, J. Liu, L. Zhang, L. Pi, Y. Zhang, and H. Yang, Sci. Rep. **6**, 14 (2016).

[21] H. P. Yang, L. Shi, S. M. Zhou, J. Y. Zhao, L. F. He, and Y. B. Jia, J. Phys.: Condens. Matter. **21**, 046002 (2009).

[22] C. Kittel, Phys. Rev. **73**, 155 (1948).

[23] C. Mellinger, J. Waybright, X. Zhang, C. Schmidt, and X. Xu, Phys. Rev. B **101**, 014413 (2020).

[24] V. Likodimos and M. Pissas, Phys. Rev. B **76**, 024422 (2007).
[25] L. Shen, G. Lan, L. Lu, C. Ma, C. Cao, C. Jiang, H. Fu, C. You, X. Lu, Y. Yang, L. Chen, M. Liu, and C. Jia, Adv. Sci. **5**, 1800855 (2018).
[26] P. G. Gowtham, G. M. Stiehl, D. C. Ralph, and R. A. Buhrman, Phys. Rev. B **93**, 024404 (2016).
[27] B. Peng, Z. Zhou, T. Nan, G. Dong, M. Feng, Q. Yang, X. Wang, S. Zhao, D. Xian, Z. Jiang, W. Ren, Z. Ye, N. X. Sun, and M. Liu, ACS Nano **11**, 4337 (2017).
[28] P. E. Blöchl, Phys. Rev. B **50**, 17953 (1994).
[29] G. Kresse and J. Furthmüller, Phys. Rev. B **54**, 11169 (1996).
[30] J. Paier, R. Hirschl, M. Marsman, and G. Kresse, J. Chem. Phys. **122**, 234102 (2005).
[31] J. P. Perdew, K. Burke, and M. Ernzerhof, Phys. Rev. Lett. **77**, 3865 (1996).
[32] D. Pesquera, G. Herranz, A. Barla, E. Pellegrin, F. Bondino, E. Magnano, F. Sanchez, and J. Fontcuberta, Nat. Commun. **3**, 1189 (2012).